AIAA Propulsion and Energy Forum
August 9-11, 2021, VIRTUAL EVENT
AIAA Propulsion and Energy 2021 Forum

10.2514/6.2021-3400

Equivalent Circuit Model for a Rotating Magnetic Field Thruster

Joshua M. Woods*, Christopher L. Sercel†, Tate M. Gill ‡, and Benjamin A. Jorns§
University of Michigan, Ann Arbor, MI, 48109

A lumped circuit model approach is used to predict performance of a rotating magnetic field (RMF) thruster. The equivalent circuit is derived by modeling the driving antennae and plasma as a collection of current loops interacting via mutual inductance and Lorentz forces. Several physically relevant assumptions are applied to reduce the complexity of the system. The resulting set of equations require five free circuit parameters that must be determined experimentally. Data from performance measurements of the Plasmadynamics and Electric Propulsion Laboratory (PEPL) RMF v2 thruster is used to calibrate the model. While the model tends to underpredict performance, it mirrors operational trends observed during the experiment. Thruster performance is discussed in the context of the fundamental scaling of the model as well as the individual scaling of the free parameters. Several methods for increasing performance are proposed, including ncreasing specific energy, flow rate, and background magnetic field strength to achieve higher impulse and efficiency.

Nomenclature

B	=	magnetic field
C	=	capacitance
e	=	elementary charge
E	=	electric field
E_0	=	input energy
E_P	=	energy deposited into plasma
f	=	pulse frequency
F_z	=	axial force
g	=	current density distribution function
j	=	plasma current
I	=	total current or total impulse
KE	=	kinetic energy
L	=	inductance
M	=	mutual inductance
$\dot{m}$	=	mass flow rate
m_s	=	mass of plasma slug
n	=	plasma density
P	=	total power
R	=	resistance
T	=	thrust
u_{ex}	=	exhaust velocity
V	=	voltage
α	=	acceleration coefficient
η	=	resistivity
Γ	=	electrical gyrators
Ω	=	Hall parameter

*PhD Candidate, Department Name, 1320 Beal Ave, Ann Arbor, MI 48109, AIAA Student Member
†PhD Candidate, Department Name, 1320 Beal Ave, Ann Arbor, MI 48109, AIAA Student Member
‡PhD Candidate, Department Name, 1320 Beal Ave, Ann Arbor, MI 48109, AIAA Student Member
§Assistant Professor, Aerospace Engineering, 1320 Beal Ave, Ann Arbor, MI 48109, AIAA Associate Fellow

ω	=	rotating magnetic field frequency
ω_{ce}	=	electron cyclotron frequency
ν_{ei}	=	electron-ion collision frequency
τ	=	ionization time constant
z_0	=	stroke length

I. Introduction

The rotating magnetic field (RMF) thruster is a novel propulsion concept that has the potential to fill the niche of high power (>100 kW) electric propulsion (EP). The concept originated in the fusion community as a method for producing and sustaining plasmoids for fusion purposes [1–3]. In recent decades, the RMF's unique method for generating azimuthal currents was adapted for propulsion purposes. As a type of inductive pulsed plasma thruster (IPPT), the RMF thruster is theoretically able to obtain a specific mass of 0.05 kg/kW, which is several orders of magnitude lower than state-of-the-art EP devices such as Hall and Gridded Ion thrusters which currently have power densities of 2 kg/kW [4]. Like other electromagnetic thrusters, the thrust of IPPTs tends to scale quadratically with coil current J. Pulsing allows IPPTs to access the high powers necessary to generate the large transient coil currents required to ionize neutrals and accelerate the plasma [5]. In addition, the inductive nature of the thruster means that there are no plasma-wetted electrodes, which significantly reduces the possibility of lifetime-limiting erosion processes. A key benefit of IPPTs is the capability to tune each pulse to a set efficiency and specific impulse, allowing us to vary thrust by changing the duty cycle. This gives the thruster a wide range of throttleability while retaining desired performance characteristics [6].

The RMF thruster is typically classified as a subclass of IPPTs called a field-reversed configuration (FRC) thruster. FRCs use azimuthal currents to drive a magnetic field opposed to a steady bias field. This produces a self-contained, magnetized body called a plasmoid. The plasmoid is accelerated out of the thruster at high speeds and pulse rates to produce thrust. FRCs have certain advantages over other IPPTs such as pulsed inductive thrusters (PITs) in that they can achieve superior mass utilization by confining the plasma during ejection. There also tends to be a longer stroke length, the distance over which the plasma remains coupled and accelerates [7]. The RMF builds upon the FRC concept by introducing an azimuthal current generation via rotating magnetic fields, which introduces favoring scaling properties related to the necessary current and voltages needed to operate the thruster. While a plasmoid might not always form, the principal of operation remains the same. Typical IPPTs, including most FRCs, require 10s of kV to induce the large currents necessary for ionization and acceleration. The RMF thruster is unique in that it relies on sinusoidal currents, which can be driven continuously and at lower voltages. Thus, induced current in the plasma comes not from large, transient currents but rather the frequency at which the current is driven [8].

Despite the theoretical advantages of the RMF thruster, available experimental data indicates poor performance. A study by Weber et. al at the University of Washington and Mathematics Sciences Northwest calculated an overall thruster efficiency of 8% for an RMF thruster operating on nitrogen at 46 J per pulse [9]. A study by Woods et. al at the University of Michigan's Plasmadynamics and Electric Propulsion laboratory (PEPL) used a similar thuster design as Weber to obtain the first published direct thrust measurements (i.e. with a thrust stand). The results again showed poor performance with coupling efficiencies of less than 5% and negligible thrust while operating up to 1.1 kW [10]. A recent follow-up study by PEPL with a redesigned thruster based on lessons learned from the previous campaign reported improved performance [11]. The thruster was operated at 5 kW. Thrust in the low 10's of mN was measured at efficiencies of 5% or less. The full results have been published alongside this study [12].

To date, several models exist that attempt to explain the underlying mechanisms of the RMF thruster. Hugrass and Jones utilized a numerical simulation coupled with a circuit analysis to study the coupling of an RMF to a fixed plasma [3]. Although this was for fusion purposes, and thus lacked the acceleration mechanisms, their work has provided valuable insight into the penetration characteristics of the RMF current drive. Weber used an enthalpy model to break down the various efficiency loss mechanisms. Using the model, he was able to approximately calculate how much energy deposited into the plasma was being lost due to ionization, radiation, convection, screened RMF energy, and unused thermal energy. Of these, radiation was the dominant loss mechanism and accounted for 78% of the total plasma energy [9, 13]. Little et al. utilized a circuit model to further understand the neutral entrainment properties of RMF thrusters when a second stage θ-pinch-like accelerator is added. In this configuration, the second stage imparts additional kinetic energy into a plasmoid already formed and partially accelerated by an RMF [14]. Finally, Woods et. al. again used a circuit analysis to directly model the coupling of the plasma's magnetic flux to the RMF antennae. The numerical model is able to recover performance trends over various operating conditions, although it remains unvalidated and complicated [15, 16]. Each of these models are not predictive, complicated, or do not model the RMF driven acceleration in the thruster. The need for a simple, predictive model is thus apparent to better understand RMF thruster performance and identify strategies for improving it.

The goal of this work is to put forth a mid-fidelity equivalent circuit model for RMF thrusters that accurately describes the underlying physics of the system while remaining simple enough to provide insight into thruster performance and optimization. We achieve this by deriving a model using a lumped circuit approach that consolidates many of the complex geometrical features of the thruster into physically intuitive circuit parameters. The lumped circuit approach has been leveraged before to model other IPPTs such as the PIT, θ-pinch FRC thrusters, and annular FRC thrusters [17–19]. To this end, this paper is organized in the following way. In section II we review operating principles of the RMF thruster and leverage these insights to derive the model. In section III, we provide an overview of a recent PEPL RMF thruster study from which we use the data to validate our model (full experimental study is found in Ref. [12]). In section IV, we use the data from the experiment to calibrate our model. In section V, we discuss the observed performance trends and how the scaling of the various free parameters can be used to further optimize design. Finally, in section VI, we conclude our study with a brief overview of key findings.

II. Theory

Here, we review the principle of RMF operation and use the mechanics to derive a lumped circuit model.

A. Idealized Model

We first overview the principle of operation of current drive through RMF thrusters. This model is based on the derivation first presented by Blevin and Thonemann [1]. The key elements in the formation process are illustrated in Fig. 1. Neutral gas with a small amount of seed plasma from a pre-ionizer fills the discharge chamber. This plasma is confined by a steady background magnetic field with a radial gradient, given in cylindrical coordinates as

$$\mathbf{B}_s = B_{s,r}\hat{\mathbf{r}} + B_{s,z}\hat{\mathbf{z}}, \tag{1}$$

where B_s denotes the steady background magnetic field and $B_{s,r}$ and $B_{s,z}$ are its radial and axial components respectively.

Two sets of saddle coils are oriented perpendicular to each other, and phase-shifted currents with frequency ω are driven through these coils, generating alternating magnetic fields that are 90° out of phase. The combined effect of these coils creates a RMF of the form

$$\mathbf{B}_{RMF} = B_o \cos(\omega t)\hat{\mathbf{x}} + B_o \sin(\omega t)\hat{\mathbf{y}}, \tag{2}$$

where B_o is the amplitude of the magnetic field. While a real RMF would have spatial variation, this idealization of the field does not. The RMF frequency should be much greater than the ion cyclotron frequency but much less than the electron cyclotron frequency to ensure that the induced ion currents are much smaller than the electron currents. The combination of Faraday's law of induction and the generalized Ohm's law for an infinitely long plasma column show that the time-varying RMF magnetic field produces an electric field that in turn drives an azimuthal plasma current. The electron Hall parameter is defined as $\Omega_e = B_o/(\eta n_e e)$, where η is the plasma resistivity, n_e is the electron density, and e is the elementary charge. In the limit of low plasma resistivity, Ω_e will be much greater than one, and the electrons will rotate in sync with the RMF. In this case, the plasma current density as a function of radial position is

$$j_\theta(r) = -n_e e \omega r, \tag{3}$$

where n_e is assumed constant. The above formulation, specifically Eq. (3), illustrates a key advantage of RMF thrusters. In principle, if the resistivity is sufficiently low, the current that is driven in the azimuthal direction is independent of the current in the driving coils.

There have been three theories proposed as to what process accelerates the plasma in the RMF thruster. A self-field acceleration component may contribute to thrust. It can be caused by a self-induced radial magnetic field interacting with the azimuthal current. Thrust may also be produced through the conversion of thermal to kinetic energy via adiabatic expansion. Here, we only consider the Lorentz force on the plasma is produced by the interaction of the azimuthal current and the external magnetic field. This equation can be expressed as

$$F_z = \int_V J_\theta B_{s,r} dV. \tag{4}$$

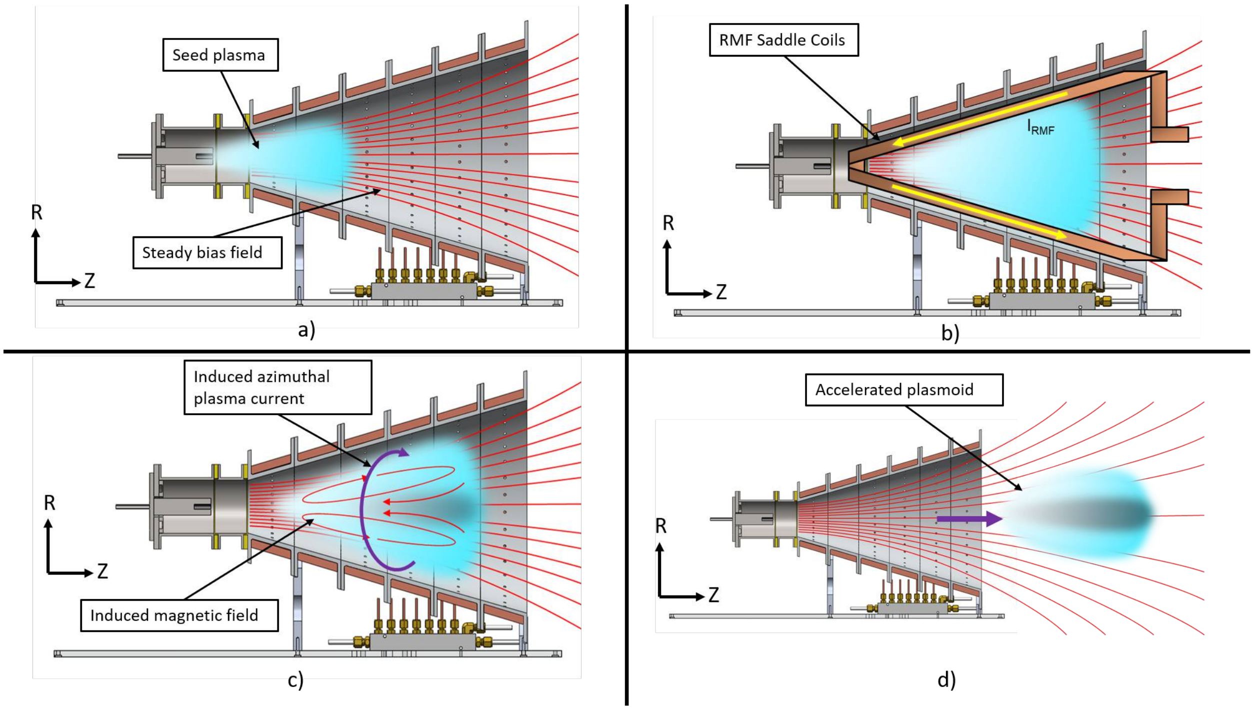

Fig. 1 RMF Operation: a) Side view cross-section in the r-z plane of the thruster illustrating how ionized gas is injected into the discharge chamber. A steady bias magnetic field with radial gradient is present. b) The RMF coils are discharged. c) An azimuthal current is generated in the plasma, which also induces an opposing magnetic field. d) The plasma is accelerated out of the thruster.

Despite this simple representation avoiding many of the intricacies related to coupling between the plasma and antennae, we can begin to see what parameters are important for thruster performance. Notably, the thrust, like the azimuthal current, scales with frequency instead of magnetic field strength. In theory, we should arrive to similar conclusions once we derive the lumped circuit model.

B. Lumped Circuit Model

Armed with fundamental operating principles outlined in the above subsection, we can begin to assemble our lumped circuit model.

1. Geometry and Assumptions

For simplicity, we assume the plasma has a cylindrical shape and is semi-infinite in length (i.e. length $\gg$ radius). The coils are arranged in a similar way to the setups shown in Fig. 3. One coil produces a magnetic field primarily in the x-direction and the other produces a field primarily in the y-direction. Other assumptions are:

- Constant plasma slug geometry
- Negligible thermal effects
- Electrons are inertialess
- Ions do not contribute to current
- Negligible electron pressure

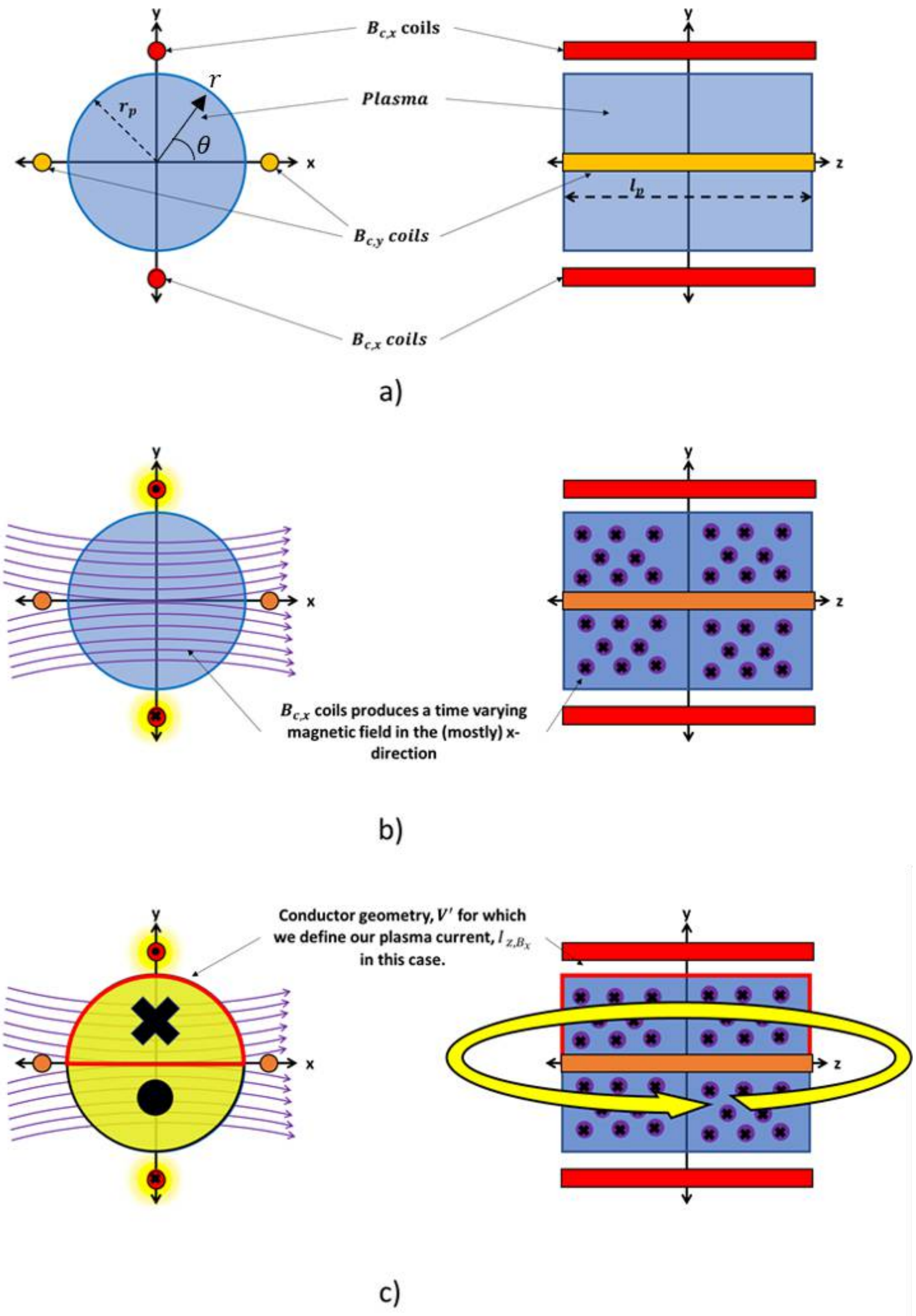

Fig. 2 Generation of axial current due to x-direction coils. End on view is on the left while a side view is featured on the right.

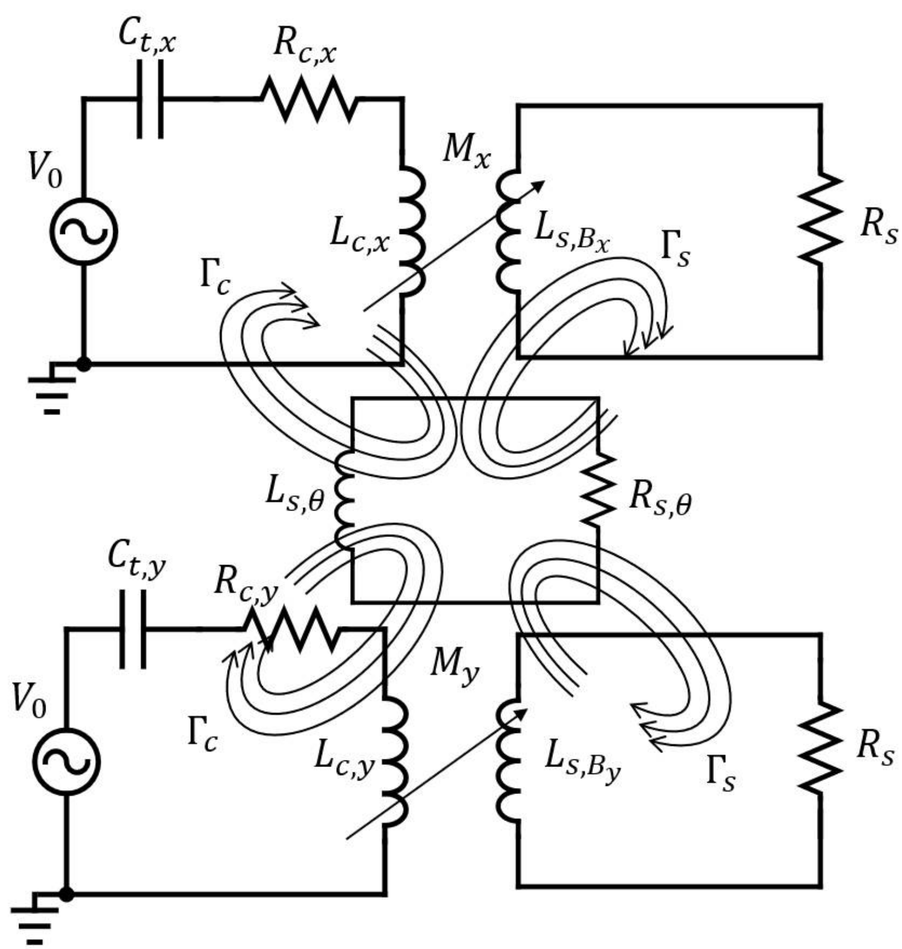

Fig. 3 RMF thruster circuit diagram. The antennae current loops are are on the left, the axial plasma current loops are on the right, and the azimuthal plasma current loop is in the center. They are all coupled inductively or through gyrator terms.

2. Deriving Axial Plasma Current Loop Equations

The two antennae couple to the axial currents in the plasma. We can use Ohm's law to describe the axial plasma currents induced in the plasma by the coils,

$$E_z - \frac{J_\theta B_r}{ne} = \eta J_z. \tag{5}$$

Here, E_z is the axial electric field, B_r is the radial magnetic field, and J_z and J_θ are the z- and θ-direction plasma current densities respectively. The coil magnetic fields are,

$$B_{c,x} = \gamma_{c,x} I_{c,x} \tag{6}$$
$$B_{c,y} = \gamma_{c,y} I_{c,y}. \tag{7}$$

The γ terms are geometric factors that relate the coil currents to the magnetic fields they produce. They are a function of r and θ. Similarly, the plasma slug creates magnetic fields due to the mirror currents induced in it by the coils,

$$B_{s,x} = \gamma_{s,x} I_{s,B_x} \tag{8}$$

$$B_{s,y} = \gamma_{s,y} I_{s,B_y}. \tag{9}$$

There is also an external, steady magnetic field,

$$\vec{B}_{ext} = B_{ext,r}\vec{r} + B_{ext,z}\vec{z}. \tag{10}$$

Thus, the total magnetic field, written in cylindrical coordinates, is

$$B_r = \left(B_{c,x} + B_{s,x}\right)\cos\theta - \left(B_{c,y} + B_{s,y} + B_{ext,y}\right)\sin\theta + B_{ext,r} \tag{11}$$

$$B_\theta = \left(B_{c,x} + B_{s,x} + B_{ext,x}\right)\sin\theta + \left(B_{c,y} + B_{s,y}\right)\cos\theta. \tag{12}$$

Per Faraday's law, time varying magnetic fields will produce electric fields. For our case, we can relate the azimuthal magnetic fields to the axial electric field,

$$\frac{\partial E_r}{\partial z} - \frac{\partial E_z}{\partial r} = -\frac{dB_\theta}{dt}. \tag{13}$$

Applying the semi-infinite plasma column assumption (all axial derivatives go to zero) and solving for E_z yields

$$E_z = \frac{\partial}{\partial t}\int B_\theta \sin\theta dr. \tag{14}$$

The magnetic and electric fields we defined can be inserted into the axial Ohm's law in Eq. 5. We have the axial current density, however, in order to obtain Kichoff's voltage law (KVL) equations for the plasma, we need to consider the plasma current that couples to each of the coils. Per Fig. 3, the x-coil produces a magnetic field in the x-direction. It couples into the plasma, driving a current in the axial direction. That resulting plasma current induces its own x-direction magnetic field that couples back to the coils. We can define a conductor geometry per Fig. 3c) which illustrates the plasma current that couples to the coil. Thus, generally speaking, there are two current density populations driven by the coils, one with a density distribution g_{z,B_x} and the other g_{z,B_y}. In addition, there is an azimuthal current density distribution function, g_θ. They are related to the plasma's total and density currents by

$$J_{z,B_x} = g_{z,B_x} I_{z,B_x} \tag{15}$$

$$J_{z,B_y} = g_{z,B_y} I_{z,B_y} \tag{16}$$

$$J_\theta = g_\theta I_\theta. \tag{17}$$

KVL for the axial plasma currents induced by the x-direction coils can be found by multiplying Eq. 5 by g_{z,B_x} and integrating over the column of the plasma, V'. The same process can be done using g_{z,B_y} to derive KVL for the axial plasma currents driven by the y-direction coils. The derivation for both equations can be found in the appendix. Here, we note the electrical parameters we obtain. We use the expressions related to the I_{z,B_x} current loop. However, they are the same apart from phase differences for I_{z,B_y}. First and foremost, there is a mutual inductance term that characterizes the coupling between the antennae and the currents. It has the form,

$$M_x = \int_{V'} g_{z,B_x} \int \gamma_{c,x} \sin\theta dr dV'. \tag{18}$$

The mutual inductance is solely a function of the geometry. Similarly, the self-inductance is

$$L_{s,B_x} = \int_{V'} g_{z,B_x} \int \gamma_{s,x} \sin\theta dr dV', \tag{19}$$

and also depends only on geometry. The resistance is the bulk analog to the plasma resistivity,

$$R_{s,B_x} = \int_{V'} \eta {g_{z,B_x}}^2 dV'. \tag{20}$$

To characterize the Lorentz force interactions within the plasma, a series of quantities called, "gyrators," are introduced. In electronics, gyrators are the fifth circuit element after resistors, capacitors, inductors, and transformers. If we suppose a current loop with voltage V_1 and current I_1, a current can be induced in another inductor with voltage V_2 and current I_2 through an ideal gyrator, G, by the equations,

$$V_1 = -GI_1 \tag{21}$$

$$V_2 = GI_2, \tag{22}$$

where G has units of resistance. In induction motors, for instance, the gyrator term manifests as the angular frequency induced by stator on the rotor [20]. In our model, the gyrator term descries how the axial plasma currents can induce azimuthal plasma currents and vice versa. For example, the gyrator term describing the interaction between I_{z,B_x}, $B_{c,x}$, and I_θ is,

$$\Gamma_{c,x}{}' = \int_{V'} \frac{g_{z,B_x} g_\theta}{ne} \gamma_{c,B_x} \cos\theta. \tag{23}$$

This gyrator term contains geometric elements related to the axial and azimuthal plasma currents. It also scales inversely with the plasma density. The gyrator parameters have units of either Ω/A or Ω/A^2 depending on whether the magnetic field in question is steady (i.e. the external fields) or depends on the coil or plasma currents respectively.

3. Deriving Azimuthal Plasma Current Loop Equations

KVL for the azimuthal plasma current can be found in much the same way as the axial plasma currents. We start with the generalized Ohm's law for the azimuthal current density,

$$E_\theta + \frac{J_z B_r}{ne} = \eta J_\theta \tag{24}$$

E_θ is only composed of the time varying electric field caused by the time varying axial magnetic field produced by the azimuthal current,

$$E_\theta = -\frac{\partial}{\partial t}\frac{1}{r}\int r B_{s,z} dr = -\frac{\partial}{\partial t}\frac{1}{r}\int r \gamma_{s,z} I_\theta dr. \tag{25}$$

We insert our previous definitions for the plasma current densities and magnetic fields, multiply by g_θ, and integrate over V' to recover KVL for the azimuthal current. In addition to recovering many of the same gyrator parameters we see in the axial plasma current KVL equations, we also obtain new electrical parameters that characterize the effective resistance caused by the magnetic fields. For instance, the resistance caused by the x-coil magnetic field is,

$$R''_{B_{c,x}} = \int_{V'} \Omega''_{B_{c,x}}{}^2 \eta g_\theta{}^2 dV', \tag{26}$$

where $\Omega''_{B_{c,x}}$ is an effective Hall parameter,

$$\Omega''_{B_{c,x}}{}^2 = \frac{\gamma_{c,B_x}{}^2 \cos\theta^2}{(\eta ne)^2}. \tag{27}$$

Like the gyrator terms, these resistances have units of either Ω/A or Ω/A^2 depending on whether the magnetic field in question is steady (i.e. the external fields) or depends on the coil or plasma currents respectively. A full list of these electrical parameters is provided in the appendix.

4. Slug Acceleration

The acceleration of the slug is defined by Newton's second law. The force acting on the slug is the Lorentz force caused by the azimuthal current interacting with the external radial magnetic field,

$$m_s \frac{d^2 z}{dt^2} = \int_{V'} B_{r,ext} g_\theta dV' I_\theta. \tag{28}$$

Here, z is the axial position of the slug and m_s is its mass. There may also be a self-induced radial magnetic field caused by the plasma coupling to flux conservers. These structures act to sustain the constant flux on the short timescales of the plasma acceleration. They consist either of metallic straps placed along the thruster cone or the cone itself is composed of conductive material [16]. In our model, flux conservers are absent as a recent study by Sercel et al. concluded that any additional coupling between the plasma and surrounding structures is an inherent loss mechanism [11]. Consequently, the thruster we use to calibrate the model is constructed of primarily nonconductive materials. Thus, the self-induced fields are minimal.

5. Antennae Current Loops

In addition to the KVL and acceleration equations, the expressions governing the forced oscillation of the antennae to produce the necessary sinusoidal waveforms are,

$$V_{C_{t,x}} + L_{c,x}\frac{dI_{c,x}}{dt} + R_{c,x}I_{c,x} - \frac{dM_{c,x}}{dt}I_{z,B_x} - M_{c,x}\frac{dI_{z,B_x}}{dt} = V_0\cos(\omega t) \tag{29}$$

$$V_{C_{t,y}} + L_{c,y}\frac{dI_{c,y}}{dt} + R_{c,y}I_{c,y} - \frac{dM_{c,y}}{dt}I_{z,B_y} - M_{c,y}\frac{dI_{z,B_y}}{dt} = V_0\sin(\omega t) \tag{30}$$

$$\frac{dV_{C_{t,x}}}{dt} = \frac{I_{c,x}}{C_{t,x}} \tag{31}$$

$$\frac{dV_{C_{t,y}}}{dt} = \frac{I_{c,y}}{C_{t,y}}. \tag{32}$$

Here, V_0 is the power supply voltage. Each of the antennae has a self-inductance, $L_{c,i}$, resistance, $R_{c,i}$, tuning capacitance, $C_{t,i}$, and mutual inductance term chracterizing coupling to the plasma, $M_{c,i}$. Here, i is either x or y depending on the antenna.

C. Simplifying the Model

The full system of equations is provided in the appendix. Without simplification, there are 34 free parameters (everything related to the plasma) across 8 equations, a remarkably convoluted system. We can reduce the number of free parameters by applying a series of physically relevant assumptions.

- **Equivalent geometric factors:** Assuming axisymmetry, the circuit parameters for quantities in the x-direction will be the same as those in the y-direction. The primary difference is a change of sign depending on the direction. As an example, we can assume the axial plasma inductances are,

$$L_{s,B_x} = L_{s,B_y} = L_s. \tag{33}$$

- **Current phase offsets:** For both the antenna and plasma axial currents, the currents associated with the y-direction magnetic fields can be expressed as constant phase offsets relative to the currents associated with the x-direction magnetic fields.

$$I_{c,y} = I_{c,x}e^{i\frac{\pi}{2}} \tag{34}$$

$$I_{z,B_y} = I_{z,B_x}e^{i\frac{\pi}{2}}. \tag{35}$$

- **Negligible plasma self-inductance:** The plasma self-inductance is low enough that the voltages induced by it are negligible relative to the other terms.
- **Negligible external field effects on driven current**: The current induced by the external magnetic field is neglibile relative to those induced by the RMF. That is,

$$B_{ext} \ll B_{RMF}. \tag{36}$$

- **Large Hall parameters:** We assume the electrons are fully magnetized to the rotating magnetic field. This causes the Hall parameter related resistances in the azimuthal KVL current loop equation to dominate.

- **Ionization time constant**: At the beginning of the discharge, most of the particles are neutrals. As current flows through the antennae, the neutrals are ionized over a finite time scale. This ionization time is assumed to be rapid, and the plasma density can be defined as

$$n_e = n_{e,f}\tanh\left(\frac{t}{\tau}\right), \tag{37}$$

where $n_{e,f}$ is the final plasma density and τ is a characteristic time constant. As a result, I_θ requires time to ramp up as more free electrons are produced and entrained by the RMF.
- **Exponentially decaying coupling:** We assume the coupling decays over some length scale as the plasma accelerates away from the thruster. The decay is represented by $e^{-\frac{z}{z_0}}$, where z_0 is a characteristic stroke length.

Applying the assumptions and reducing the equations yields the following,

$$\begin{aligned}\left(L_{c,x} - M_{0,eff}\,e^{-\frac{z}{z_0}}\right)\frac{d^2 I_{c,x}}{dt^2} + \left(R_{c,x} - 2\frac{d\left(M_{0,eff}\,e^{-\frac{z}{z_0}}\right)}{dt}\right)\frac{dI_{c,x}}{dt} \\ + \left(\frac{1}{C_{t,x}} + \frac{d^2\left(M_{0,eff}\,e^{-\frac{z}{z_0}}\right)}{dt^2}\right) I_{c,x} = \omega V_0 \sin(\omega t)\end{aligned} \tag{38}$$

$$m_s\frac{d^2 z}{dt^2} = \alpha\,(1-i)\left[\frac{\frac{dI_{c,x}}{dt}}{I_{c,x}} - \frac{2}{z_0}\frac{dz}{dt} - \frac{R_s}{M_{0,eff}}\right]\tanh\left(\frac{t}{\tau}\right)e^{-\frac{z}{z_0}}. \tag{39}$$

Here we have collapsed our original system of 8 to 2. The free parameters are a characteristic mutual inductance, $M_{0,eff}$; the stroke length, z_0; the plasma resistance, R_s; the ionization time constant, τ; and an acceleration constant, α. The coil inductance, capacitance, and resistance can be measured. V_0 and ω are parameters set by the operator. The first equation represents the antenna current. The inductance, resistance, and capacitance terms have been modified by mutual inductance expressions relating how each quantity is perturbed by the plasma. Each of these quantities decays exponentially as the slug is ejected from the thruster. The second equation is the acceleration of the slug. m_s is the mass of the neutrals initially present in the thruster cone. The terms in the brackets correspond to the azimuthal current generated in the plasma. The thrust scales with α as well as a hyperbolic tangent function related to the breakdown of theneutrals over time. Like the mutual inductances in the coil equation, the force acting on the slug decays exponentially. Our system stands in contrast to other circuit models, such as those of PITs, which present the coil and plasma current as separate equations [21]. Here, they have been lumped together, providing more insight into how the plasma directly interacts inductively, restively, and capacitively with the antennae.

D. Physical significance of free parameters

Despite acting as free parameters, the coefficients introduced in the previous section are grounded in the fundamental physics of the system.

- **Stroke length -** z_0**:** This parameter is a characteristic stroke length associated with the geometry of the thruster. The longer the thruster, the longer the plasma will stay coupled to the antennae. Like other IPPTs, the length of the pulse should be optimized to cease discharge once the plasma has decoupled from the driving coils [21, 22].
- **Effective mutual inductance -** $M_{0,eff}$**:** This parameter serves as a modified mutual inductance term. It consists of usual mutual inductance, commonly found derived in inductively coupled circuits, multiplied by a ratio of resistances,

$$M_{0,eff} = M\frac{R_{\Omega_c}{}'}{R_{\Omega_s}{}'}, \tag{40}$$

where M is the classical mutual inductance between the antennae and the axial plasma currents. Essentially, the larger the cone, the larger the mutual inductance resulting in greater coupling. $\frac{R_{\Omega_c}}{R_{\Omega_s}}$ reflects a ratio of Hall parameters between the coil and plasma induced radial magnetic fields,

$$\frac{R_{\Omega_c}}{R_{\Omega_s}} = \frac{\int_{V'}\Omega''_{B_c}{}^2\eta g_\theta{}^2 dV'}{\int_{V'}\Omega''_{B_s}{}^2\eta g_\theta{}^2 dV'}, \tag{41}$$

where

$$\Omega_{B_c}''^{\,2} = \frac{{\gamma_c}^2 \cos\theta^2}{(\eta n e)^2} \tag{42}$$

$$\Omega_{B_s}''^{\,2} = \frac{{\gamma_s}^2 \cos\theta^2}{(\eta n e)^2}. \tag{43}$$

Consequently, $\frac{R_{\Omega_c}}{R_{\Omega_s}}$ reduces to essentially $\frac{\gamma_c}{\gamma_s}$. The larger the γ, the less is needed to generate a given magnetic field. The larger this ratio, the higher the propensity of electrons to become entrained by the coil generated magnetic fields, thus increasing the coupling. $M_{0,eff}$ is purely a function of geometry.

- **Acceleration coefficient - α:** The acceleration coefficient lumps together the magnetic field element of the Lorentz force, the azimuthal current density distribution, the mutual inductance, and geometry,

$$\alpha = \int_{V'} g_\theta B_{r,ext} dV' \frac{M_{0,eff}}{\Gamma_{c,0} - \Gamma_s {R_0}^*}. \tag{44}$$

Greater physical insight can be gained if we consider α in the context of the entirety of the acceleration equation

$$m_s \frac{d^2 z}{dt^2} = \int_{V'} g_\theta B_{r,ext} dV' \,(1-i) \left[\frac{M_{0,eff} \frac{dI_{c,x}}{dt} - \frac{2}{z_0} M_{0,eff} \frac{dz}{dt} I_{c,x} - R_s I_{c,x}}{\left(\Gamma_{c,0} - \Gamma_s {R_0}^*\right) I_{c,x}} \right] \tanh\left(\frac{t}{\tau}\right) e^{-\frac{z}{z_0}}, \tag{45}$$

where we have substituted our definition for α and rewritten the equation in a more intuitive form. The terms in the brackets represent the azimuthal current in the plasma. The numerator is in units of V. It characterizes the axial electric fields experienced by the plasma. The denominator is the gyrator term caused by the radial magnetic fields. It has units of Ω. Physically, this ratio represents an $E \times B$ drift. Thus, α lumps together the external radial magnetic field, geometry, and geometric scaling related to the $E \times B$ drift that results in the azimuthal plasma current. Indeed, if we assume sinusoidal currents, we can rewrite 45 as,

$$m_s \frac{d^2 z}{dt^2} = \alpha\,(1-i) \left[\omega - \frac{2}{z_0} \frac{dz}{dt} - \frac{R_s}{M_{0,eff}} \right] \tanh\left(\frac{t}{\tau}\right) e^{-\frac{z}{z_0}}, \tag{46}$$

where we see that the thrust, and thus the azimuthal current, scales linearly with the RMF frequency. This result parallels the simplified current density expression discussed at the beginning of this section which showed j_θ scaling with ω as well. Thus, the acceleration is independent of the magnitude of the RMF assuming it is strong enough to fully entrain the electrons (i.e. the Hall parameters are large).

- **Ionization time constant - τ:** As the antennae discharge into the plasma, more neutrals will become ionized. The process will be rapid but finite. The higher the ionization fraction, the more electrons are available to be entrained by the RMF, thus increasing the Lorentz force. This phenomenon is reflected by the fact that α is proportional to the plasma density. τ is used as a characteristic ionization time.
- **Slug resistance - R_s:** R_s represents losses due principally to electron-ion, electron-neutral collisions, ionization, unused thermal energy, and radiation.

In the following section, we discuss how the waveform and other performance data were obtained before moving on to actual model calibration.

III. Experimental Setup

To determine the validity of the model outlined in Sec. II, we use performance data from the PEPL RMF thruster v2. The full details of the experiment can be found in Ref. [12]. For our purposes, we only provide a brief overview of the experimental setup to frame the methodology for calibrating the model. The thruster is shown in Fig. 4 before and during operation.

A. Thruster Test Article

The PEPL RMF thruster v2 is a 5-kW class device. It operates on xenon gas at flow rates up to 200 sccm. The thruster consists of a LaB6 hollow cathode pre-ionizer that produces into a thruster cone angled at approximately 14°.

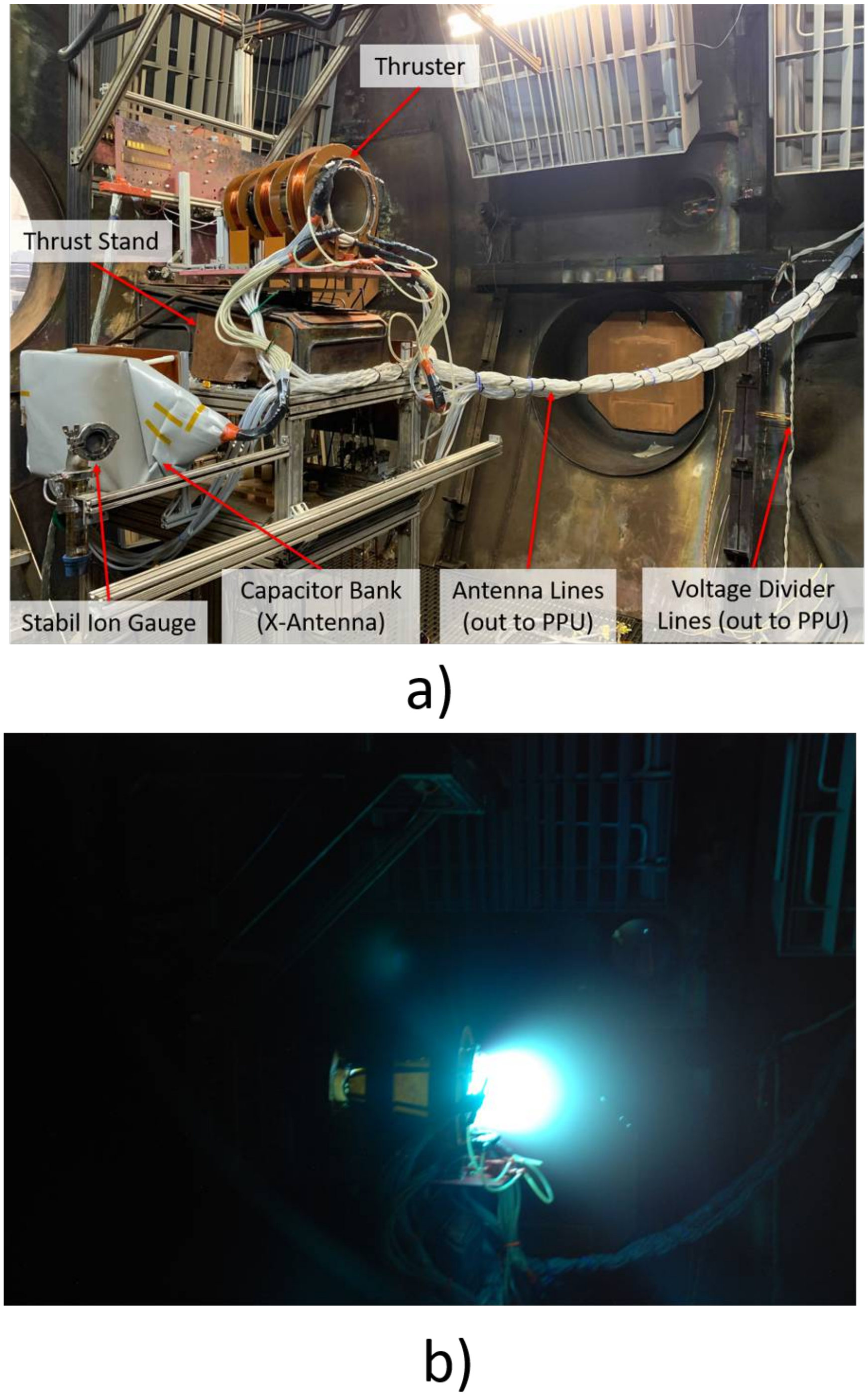

Fig. 4 a) PEPL RMF thruster v2 experimental setup b) 10 s exposure image of RMFv2 thruster operating at the 45 sccm Xe flow, 1.95 kA peak antenna curent,120 G centerline bias field condition at 75 Hz repetition rate.

Three electromagnets produce a steady diverging field. The thruster is powered by a custom pulsed power unit (PPU) built by Eagle Harbor Technologies that produces a steady waveform for each antenna with amplitudes up to 2 kA peak-to-peak. The antennae currents were measured using Pearson coils and recorded via an oscilloscope. The PPU pulses for 200 μs at 75 Hz. It can fire for approximately 5 minutes at a time before heating becomes an issue.

We measured thrust using an inverted pendulum thrust stand operating in null mode. Although originally intended for use with steady state thrusters, the stand can be operated with pulsed devices so long as its natural frequency (1-2 Hz) is significantly less than the pulse rate [23]. An optical sensor was used to measure the displacement caused by the thruster. The measurements were adjusted to account for inclination as well as EMF effects caused by the discharging antennae. All measurements were taken in the PEPL Large Vacuum Test Facility (LVTF) [24].

The experimental setup provides two critical pieces of data. The first is the thrust. Using this measurement, we can calculate the impulse and efficiency of the pulses. The impulse is calculated by dividing the measured thrust, T, by the pulse frequency, f,

$$I = \frac{T}{f}. \tag{47}$$

The kinetic energy of the accelerated plasmoid is then

$$KE = \frac{1}{2}\frac{I^2}{m_{bit}}, \tag{48}$$

where m_{bit} is the mass of the plasma in the cone at the time of discharge. The total energy discharged by the RMF antennae, E_{pulse} is

$$E_{pulse} = \frac{P}{f}, \tag{49}$$

where P is the average power. Thus, the impulse efficiency, which effectively serves as a correction for the duty cycle, is

$$\eta = \frac{KE}{E_{pulse}} = \frac{I^2 f}{2m_{bit}P} = \frac{T^2}{2m_{bit}fP}. \tag{50}$$

The second piece of data that we collect is the antenna current discharge waveform. The waveform is used to tune the model introduced in Sec. II using a least-square-fit. We discuss the procedure for this in the following section.

IV. Methodology

In this section, we provide details on how we run the model, calibrate it, and estimate performance.

A. Model Calibration

The model assumes initial current and the time derivative of the current are both zero and that the plasma slug is initially stationary at $z = 0$. The experimental waveform provides current through the x-coil as at several times over the course of the discharge. Using Mathematica, a least-square-fit is performed to match the discharge envelope from the model current to the measured current by varying the free parameters.

Initially, the coil parameters are unknown. To measure the properties, the model is first calibrated using the coil resistance, inductance, and capacitance as well as free parameters and the discharge waveform taken from a vacuum shot (i.e. not plasma-loaded). V_0 was 150 V. The fit is shown in Fig. 5. Physically, we see that the peak antenna current rings up to a certain level before remaining relatively constant over the duration of the discharge. This is expected as the PPU works to constantly oscillate the LC circuit close to resonance to produce the desired sinusoidal current. Applying our fitting procedure yields a reistance, inductance, and capacitance of 0.19 Ω, 3.4 μH, and 42 nF respectively.

Now that the antennae properties are known, we can fit the model to plasma-loaded cases. To reduce the number of free parameters, z_0 is assumed to be the characteristic length of the thruster, 0.15 m. Since it is a geometric term, we expect it to remain constant for all cases. A sample fit is shown in figure 6. The antenna current was 1.95 kA, the flow rate was 45 sccm, and there was a 80 G peak centerline background magnetic field. Here, we see that the current begins to rise before decreasing over most of the discharge. This reflects the plasma load on the circuit. After some time, the current rises again as the plasma is ejected out of the thruster. The resulting fit yielded a $M_{0,eff}$ of 298 nH, R_s of 0.79 Ω, an α of 3.6 $\times 10^{-}7 kgm/s$, and a τ of 358 μs. The calculated exhaust velocity was 1722 m/s compared to a measured value of 3242 m/s.

B. Predicted performance metrics from model

Ultimately, the goal of the model is to determine the exhaust velocity of the slug. The velocity as a function of time for the case illustrated in Fig. 6 is shown in Fig. 7. u_{ex} is the final axial velocity at the end of the pulse. The calculated exhaust velocity for this case was 1722 m/s compared to a measured value of 3242 m/s.

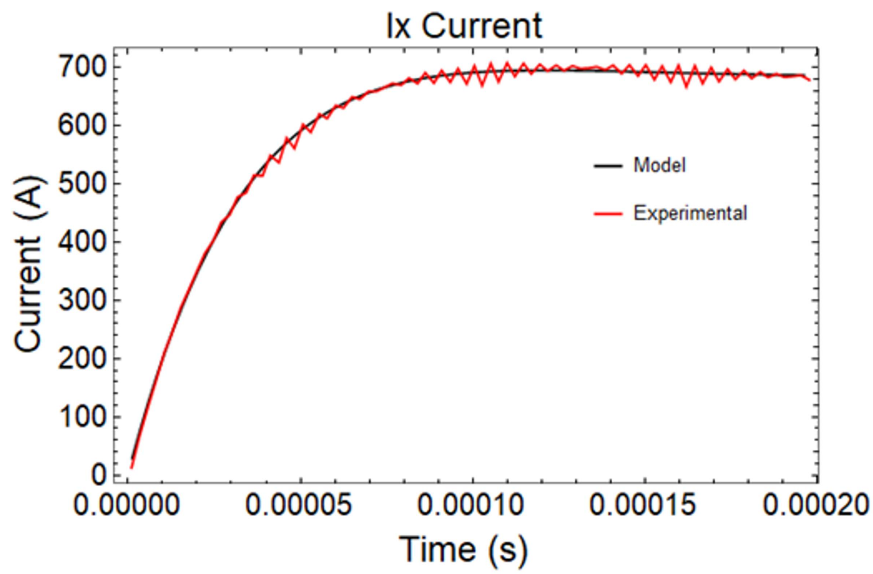

Fig. 5 Sample vacuum shot ringdown envelope at 150 V.

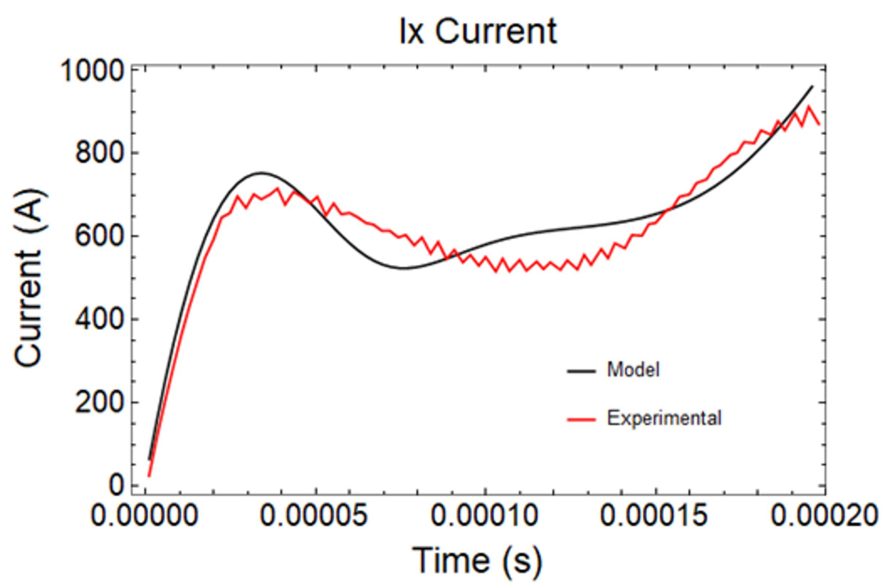

Fig. 6 Sample plasma loaded waveform for thruster operating at 1.95 kA, 45 sccm, and 80 G peak centerline magnetic field.

The impulse is then

$$I_{fit} = m_{bit} u_{ex}, \tag{51}$$

leading to a kinetic energy of,

$$KE_{fit} = \frac{1}{2} \frac{I_{fit}^{2}}{m_{bit}}. \tag{52}$$

The calculated model efficiency is

$$\eta_{fit} = \frac{KE_{fit}}{E_{pulse}}. \tag{53}$$

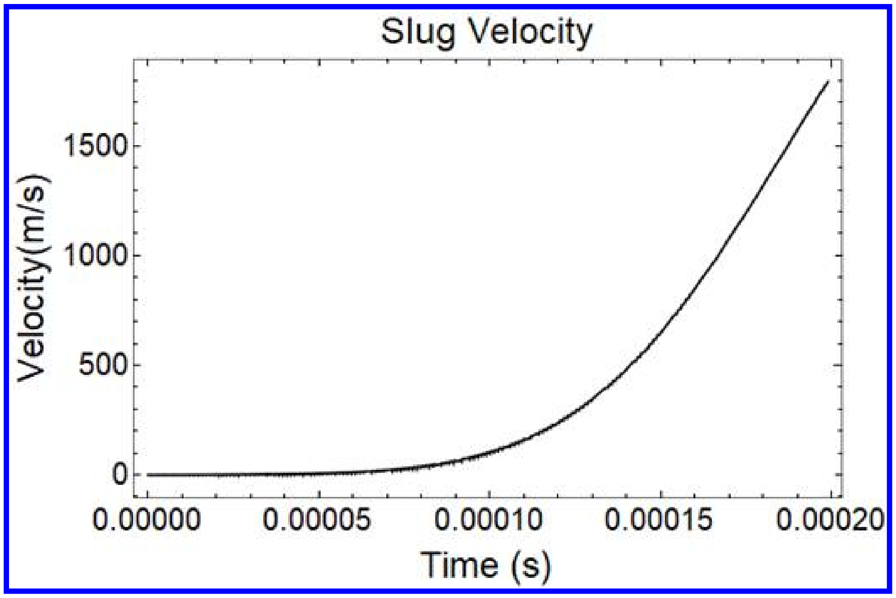

Fig. 7 Sample model slug velocity over time for thruster operating at 1.95 kA, 45 sccm, and 80 G peak centerline magnetic field.

We can compare the experimental and theoretical efficiency and impulse to assess the validity of our model. In the following section, we present results over a wide range of operating conditions before discussing our findings in the context of thruster performance.

V. Results

In this section, we present the results of fitting the model to thruster data obtained across a wide range of operating conditions. The flow was varied from 45 to 60 sccm with 80 and 120 G peak centerline magnetic fields. The antenna was discharged at 1.5, 1.7, and 1.95 kA, all at a 75 Hz pulse rate. Fitting the model yielded the following results for specific impulse and efficiency.

A. Fit parameters as a function of operating conditions

In Figs. 8 - 11, each fit parameter is presented as a function of flow rate, magnetic field, and peak antenna current. $M_{0,eff}$ remains relatively constant across the operating conditions. However, α, τ, and R_s tend to decrease with peak antenna current. Larger flowrates also tend to contribute to higher α, τ, and R_s.

B. Comparison to performance measurements

The model tends to underpredict specific impulse and efficiency, however, it does mirror the trends seen in the experimental data. Both the experimental data and model show that specific impulse and efficiency increase with specific energy. The implication of these trends are discussed in the following section.

VI. Discussion

In this section, we compare the model results to the the measured experimental values, discuss the dependency of the performance on the model parameters, and consider the implications of our conclusions on future RMF thruster

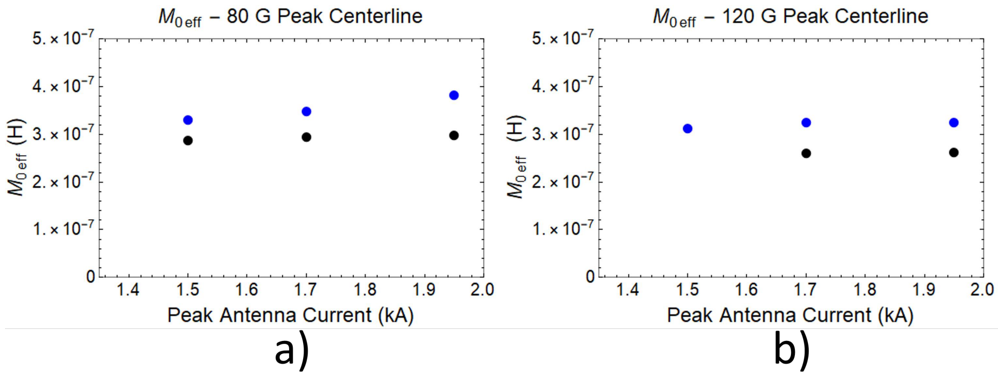

Fig. 8 $M_{0,eff}$ **as a function of flow rate and peak current at a) 80 G and b) 120 G peak centerline background magnetic field**

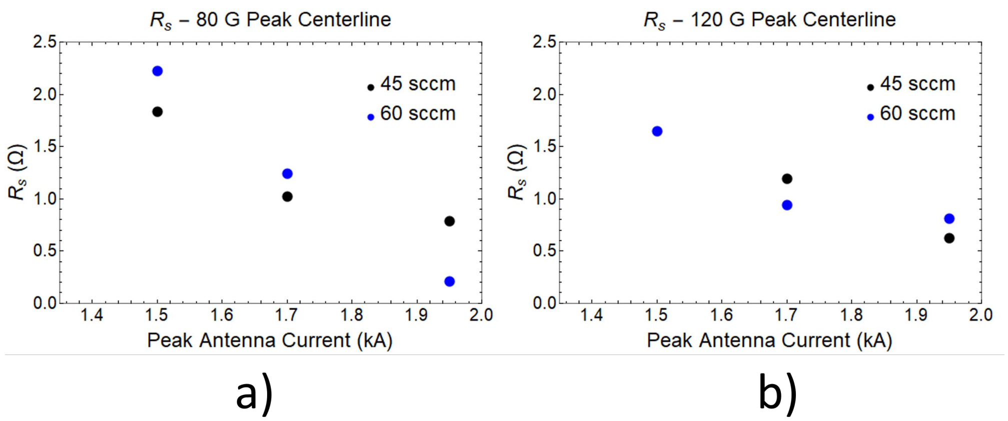

Fig. 9 R_s **as a function of flow rate and peak current at a) 80 G and b) 120 G peak centerline background magnetic field**

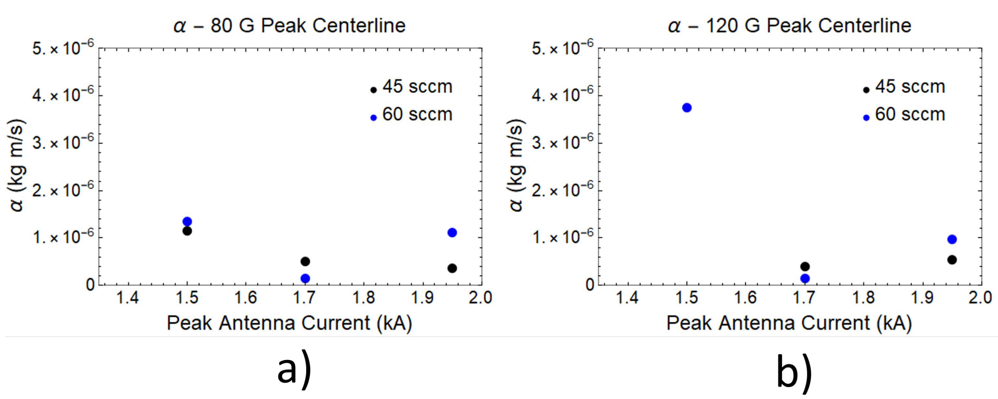

Fig. 10 α **as a function of flow rate and peak current at a) 80 G and b) 120 G peak centerline background magnetic field**

operation and design.

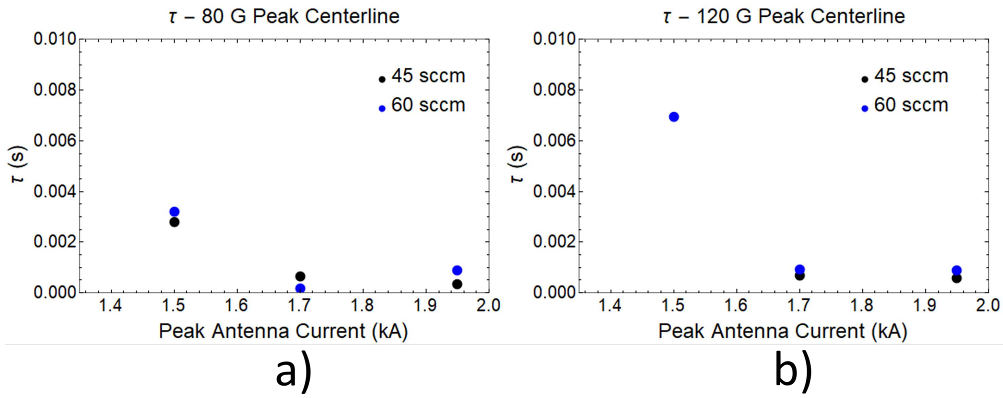

Fig. 11 τ **as a function of flow rate and peak current at a) 80 G and b) 120 G peak centerline background magnetic field**

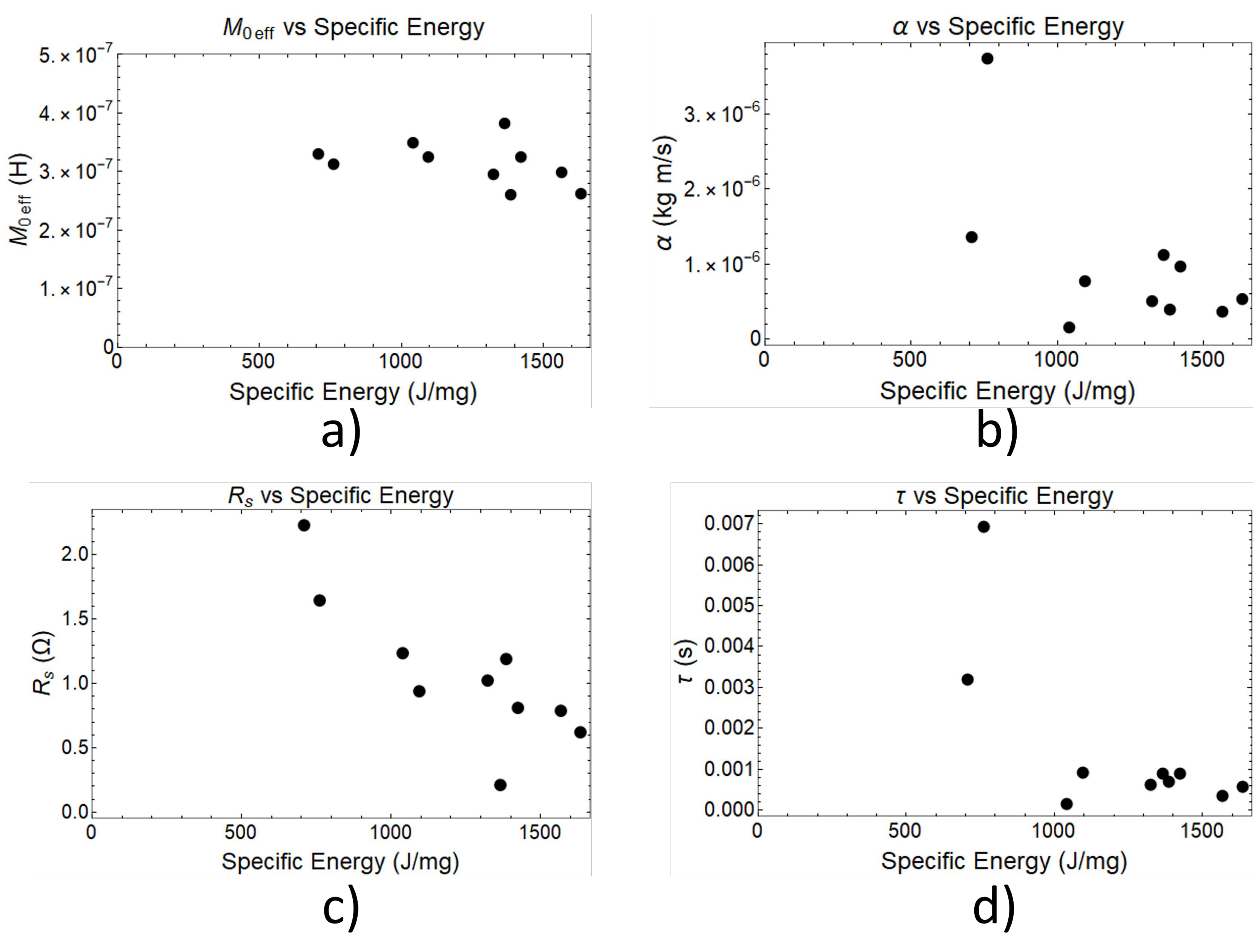

Fig. 12 Model parameters as a function of specific energy a) mutual inductance b) acceleration coefficient c) plasma resistance d) ionization time constant

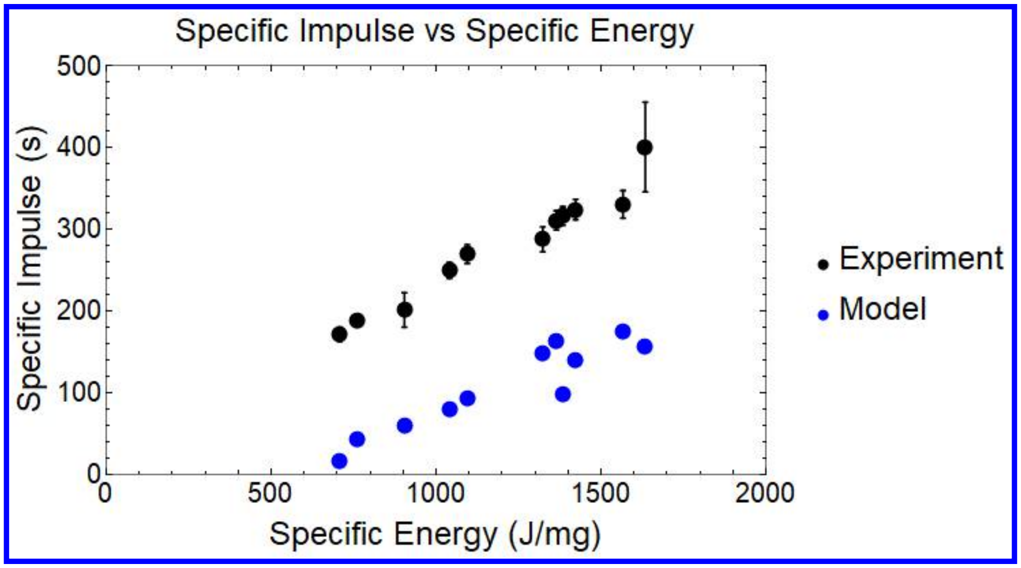

Fig. 13 Specific impulse versus specific energy for experiment and model.

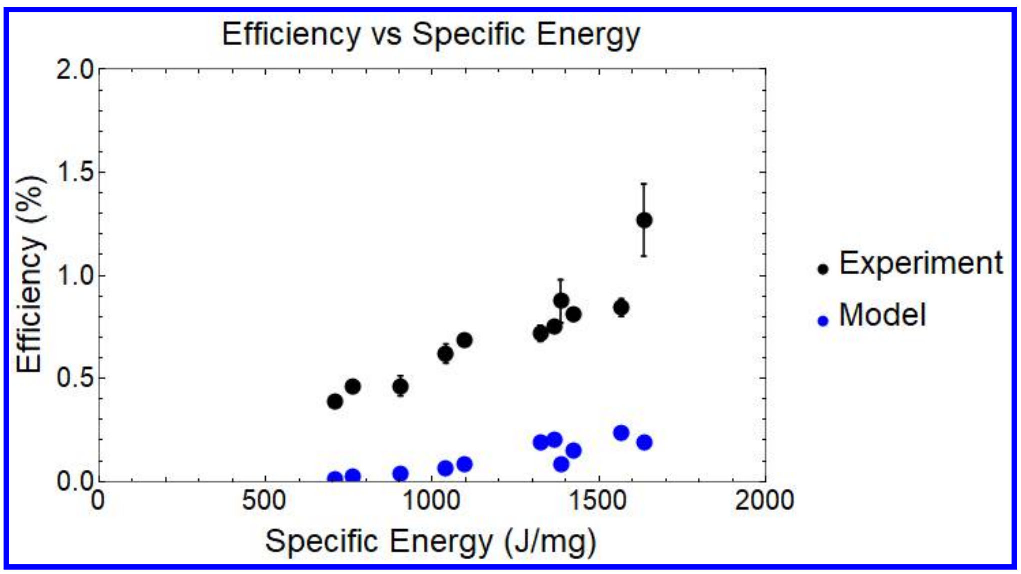

Fig. 14 Efficiency versus specific energy for experiment and model.

A. Observed trends

The specific impulse and efficiency plots show that the model consistently underpredicts performance. The lower exhaust velocity reduces the efficiency determined by the model. The discrepancy may point toward a missing acceleration mechanism. Three theories have been put forth to explain the thrust generation mechanism in RMF thrusters. The model presented in this study considers only the Lorentz force caused by the interaction between the azimuthal current and applied magnetic field. In principle, however, a self-generated radial field may also contribute to this Lorentz force. Additionally, the magnetic nozzle can convert the thermal energy into kinetic energy via adiabatic expansion. Either of these two processes can add impulse during the discharge, thus boosting the overall performance of the thruster. Previous work may also support this hypothesis. Weber calculated that the electrodless Lorentz force (ELF) thruster, operated by MSNW, was able to convert approximately 50% of the total thermal and magnetic energy deposited into the plasma by the RMF antennae into useful kinetic energy [13]. Incorporating thermal expansion into our model could close the gap we see between the theoretical and measured impulse values. Nevertheless, despite the discrepancies, the model accurately reflects the general trend presented by the experimental data that both impulse and efficiency increase with specific energy.

B. Explanation of trends in model parameters

We can extract information from the scaling of the free parameters with performance to identify potential pathways for increased performance.

- **Effective mutual inductance - $M_{0,eff}$:** $M_{0,eff}$ is a critical parameter for the operation of the thruster. It characterizes how energy is transferred from the antennae to the plasma. A larger mutual inductance represents greater coupling. Fundamentally, $M_{0,eff}$ depends on the geometry of the device as well as the current distribution in the plasma. In this study, $M_{0,eff}$ is insensitive to the operating conditions, reflecting the mutual inductance's dependency primarily on geometry of the thruster.
- **Plasma resistance - R_s:** The plasma resistance tends to be on the order of or above that of the antenna resistance. This indicates that energy is being readily coupled to the plasma but not converted to kinetic energy. This tracks with the efficiency scaling as a function of specific energy presented in Fig. 14. The plasma resistance decreases with increased specific energy. Fig. 11 shows that the plasma resistance specifically reduces with peak antennae current. Physically, this is because a higher antennae current results in better coupling with the plasma. More neutrals are ionized and the bulk plasma temperature is higher. Consequently, electron-ion and neutral collisions decrease, leading to fewer losses in the plasma.
- **Ionization time constant - τ:** Per Fig. 11, the ionization constant decreases with peak antennae current. The trend mirrors the plasma resistance. A higher current results in better coupling, and thus specific energy, which ionizes the plasma faster.
- **Acceleration coefficient- α:** Fig. 12b shows that α decreases with specific energy. Physically, this is due to α scaling linearly with plasma density. More free electrons translates to more electrons becoming entrained by the RMF, thus leading to higher thruster.

C. Pathways for Increased Performance

Using the model and the resulting fits to data, we can determine a number of ways to increase overall performance of the thruster. First, following the scaling of other IPPTs [6], the RMF thruster has increased performance for higher specific energies. The model shows that a key benefit of higher pulse energies is a faster ionization time and a lower plasma resistance. A faster ionization means more electrons will be available earlier in the pulse. These electrons will contribute to the azimuthal current necessary to produce thrust. Lower plasma resistances translate to fewer energy losses in the plasma. More energy can be coupled to the plasma by increasing the mutual inductance, which can be achieved by increasing the physical size of the thruster. Increasing the α parameter yields increased thrust. From Eq. 44, we see that the acceleration coefficient can be increased by increasing the background magnetic field strength and flow rate. Increasing the magnetic field strength is straightforward. A higher field results in a higher rate of converting the magnetic energy to directed kinetic energy. However, increasing the mass flow rate is slightly more nuanced. More mass flow will result in more thrust but will decrease specific energy. Thus, the energy must be similarly increased if specific impulse is to remain above a desired level. It is also physically possible that a pulse energy beyond what is necessary to entrain the electrons will lead to efficiency losses. Beyond this, the power input by the antennae does not contribute to the Lorentz force action. However, it likely is deposited as thermal energy which can be directed to kinetic energy via adiabatic expansion. Although the model in this study does not include this thermal-to-kinetic conversion, it would follow that the scaling should be similar to other magnetic nozzle thrusters which increase in performance with flow rate and input energy [25]. Additionally, a limitation that thus far appears to be unique to the RMF is the possibility of reversing the azimuthal current over the course of the acceleration. The acceleration is defined by a Lorentz force and is repeated here,

$$m_s \frac{d^2 z}{dt^2} = \alpha (1 - i) \left[\frac{\frac{dI_{c,x}}{dt}}{I_{c,x}} - \frac{2}{z_0} \frac{dz}{dt} - \frac{R_s}{M_{0,eff}} \right] \tanh\left(\frac{t}{\tau}\right) e^{-\frac{z}{z_0}}. \quad (54)$$

The terms in brackets define the direction of the azimuthal current. Assuming the resistance contribution is negligible, we can see that it is possible for the current to reverse if $\frac{dz}{dt}$ is large enough. Physically, this represents the change in magnetic flux being dominated by the axial translation of the slug, not the frequency of the discharge. We can define a simple operation criteria provided we substitute the exhaust velocity, u_{ex} for $\frac{dz}{dt}$,

$$u_{ex} < \frac{2}{z_0} \frac{\frac{dI_{c,x}}{dt}}{I_{c,x}} \approx \frac{1}{2} z_0 \omega. \tag{55}$$

Physically, this expressions shows that the the slug is losing energy to the RMF antennae as flux is conserved throughout the discharge. The relationship places an upperbound on achievable specific impulse and suggests the thruster needs to operate with longer geometries or higher frequencies. For our geometry and RMF frequency, the theoretical maximum achievable exhaust veloicty is 198 km/s.

Overall, the trends in the free parameters over several operating conditions coupled with the underlying physics of the model shows that increased performance can be achieved by increasing the specific power, background magnetic field, flow rate, and physical size of the thruster.

VII. Conclusion

The goal of this work is to put forth a simple model that can be calibrated against data to provide more insight into the performance scaling characteristics of RMF thrusters. To accomplish this, we derived an equivalent circuit model for the system. We used a simplified geometry consisting of a cylindrical, semi-infinite plasma slug in conjunction with Ohm's law to derive governing equations for the various current loops and how they interact with each other. Coupled with Newton's second law to describe the acceleration of the slug, a system of governing equations was derived. To reduce their complexity, we applied several physically relevant assumptions. Namely, we assumed equivalent geometric factors for the x- and y-direction coils, a constant electrical phase offset between antennae discharges, large Hall parameters, neglibible plasma self-inductance, and neglibile external magnetic field effects on driven plasma current. These assumpstions reduced the number of equations from eight to two. One equation defines the antennae current while the other describes the slug translation. There are five free parameters. The stroke length, z_0, was assumed to be fixed at 0.15 m. The rest were determined by calibrating the model from operational data using the PEPL RMF v2. The model tends to underpredict performance but mirror scaling trends. We used our model to discuss pathways for increasing performance. In particular, higher specific energies, background magnetic fields, and flow rates will all lead to increased specific impulse and efficiency. Also, a limitation for exhaust velocity was identified. u_{ex} must be below $\frac{1}{2} z_0 \omega$ lest the azimuthal current is reversed resulting in negative thrust. These scaling can help inform future thruster design.

VIII. Acknowledgements

We would like to thank Eagle Harbor Technologies for their work on developing the PPU for the thruster, Eric Viges for his assistance in fabricating the thruster and operating the facility, NASA Space Technology Research Fellowship grant number 80NSSC18K1190, and NASA Space Technology Research Graduate Opportunities grant number 80NSSC20K1168.

IX. Appendix

Here, we provide a more detailed derivation of the model.

1. Geometry and assumptions

For simplicity, we assume the plasma has a cylindrical shape and is semi-infinite in length (i.e. length $\gg$ radius). The coils are arranged in a similar way to the setups shown in Fig. 3. One coil produces a magnetic field primarily in the x-direction and the other produces a field primarily in the y-direction. Other assumptions are,

- Constant plasma slug geometry
- Neglect thermal effects
- Electrons are inertialess
- Ions do not contribute to current
- Neglect electron pressure

2. Deriving Axial Plasma Current Loop Equations

The two antennae couple to the axial currents in the plasma. We can use Ohm's law to describe the axial plasma currents induced in the plasma by the coils,

$$E_z - \frac{J_\theta B_r}{ne} = \eta J_z. \tag{56}$$

Here, E_z is the axial electric field, B_r is the radial magnetic field, and J_z and J_θ are the z- and θ-direction plasma current densities respectively. We assume that one coil produces a magnetic field purely in the x-direction while the other produces a coil only in the y-direction,

$$B_{c,x} = \gamma_{c,x} I_{c,x} \tag{57}$$
$$B_{c,y} = \gamma_{c,y} I_{c,y}. \tag{58}$$

Here, the γ terms are geometric factors that relate the coil currents to the magnetic fields they produce. They are a function of r and θ. Similarly, the plasma slug creates magnetic fields due to the mirror currents induced in it by the coils,

$$B_{s,x} = \gamma_{s,x} I_{s,B_x} \tag{59}$$
$$B_{s,y} = \gamma_{s,y} I_{s,B_y}. \tag{60}$$

There is also an external, steady magnetic field,

$$\vec{B}_{ext} = B_{ext,r}\vec{r} + B_{ext,z}\vec{z}. \tag{61}$$

Thus, the total magnetic field, written in cylindrical coordinates, is

$$B_r = \left(B_{c,x} + B_{s,x}\right)\cos\theta - \left(B_{c,y} + B_{s,y} + B_{ext,y}\right)\sin\theta + B_{ext,r} \tag{62}$$
$$B_\theta = \left(B_{c,x} + B_{s,x} + B_{ext,x}\right)\sin\theta + \left(B_{c,y} + B_{s,y}\right)\cos\theta\vec{\theta}. \tag{63}$$

Per Faraday's law, time varying magnetic fields will produce electric fields. For our case, we can relate the θ-direction magnetic fields to the axial electric field,

$$\frac{\partial E_r}{\partial z} - \frac{\partial E_z}{\partial r} = -\frac{dB_\theta}{dt}. \tag{64}$$

Applying the semi-infinite plasma column assumption (all axial derivatives go to zero) and solving for E_z yields

$$E_z = \frac{\partial}{\partial t}\int B_{c,x}\sin\theta dr + \frac{\partial}{\partial t}\int B_{s,x}\sin\theta dr + \frac{\partial}{\partial t}\int B_{c,y}\cos\theta dr + \frac{\partial}{\partial t}\int B_{s,y}\cos\theta dr. \tag{65}$$

Now, the relevant electric and magnetic fields have been defined. Consequently, our Ohm's law is now

$$\begin{aligned}\frac{\partial}{\partial t}\int B_{c,x}\sin\theta dr + \frac{\partial}{\partial t}\int B_{s,x}\sin\theta dr + \frac{\partial}{\partial t}\int B_{c,y}\cos\theta dr + \frac{\partial}{\partial t}\int B_{s,y}\cos\theta dr - \\ \frac{J_\theta}{ne}\left[\left(B_{c,x} + B_{s,x}\right)\cos\theta - \left(B_{c,y} + B_{s,y}\right)\sin\theta + B_{ext,r}\right] = \eta J_z\end{aligned}. \tag{66}$$

We have the axial current density, however, in order to obtain Kichoff's voltage law (KVL) equations for the plasma, we need to consider the plasma current that couples to each of the coils. Per figure 3, the x-coil produces a magnetic field in the x-direction. It couples into the plasma which drives a current in the axial direction. That resulting plasma current induces its own x-direction magnetic field that couples back on to the coils. We can define a conductor geometry per 3c) which illustrates the plasma current that couples to the coil. We multiply equation 66 by the axial plasma current distribution, g_{z,B_x}, and integrate over the conductor volume, V' to obtain

$$\frac{d\left(M_x I_{c,x}\right)}{dt} + \frac{d\left(L_{s,B_x} I_{c,x}\right)}{dt} - \left[\Gamma_{c,x} I_{c,x} - \Gamma_{c,(x,y)} I_{c,y} + \Gamma_{s,x} I_{s,B_{s,x}} - \Gamma_{s,(x,y)} I_{s,B_{s,y}} + \Gamma_{ext,B_x}\right] I_\theta = R_{s,B_x} I_{s,B_x}. \tag{67}$$

where M_x is the mutual inductance between the x-direction coil and the plasma, L_{s,B_x} is the plasma self-inductance for the x-direction magnetic field, R_{s,B_x} is the plasma resistance, and the Γ terms are lumped circuit terms related to the Lorentz force between the axial and azimuthal plasma currents.

The various currents have also been related to current densities by

$$J_{z,B_x} = g_{z,B_x} I_{z,B_x} \tag{68}$$

$$J_{z,B_y} = g_{z,B_y} I_{z,B_y} \tag{69}$$

$$J_\theta = g_\theta I_\theta . \tag{70}$$

Note that terms related to the mutual inductance caused by the y-coil as well as the self-inductance related by y-direction fields do not manifest in the equation. This is because those terms are related to the y-direction fields and thus integrate out. That is, they do not contribute to the current that generates the x-direction magnetic field necessary to couple with the x-coil. In fact, J_{z,B_x} is simply equation 66 without the electric field contributions from $B_{c,y}$ and $B_{s,y}$,

$$\frac{\partial}{\partial t}\int B_{c,x}\sin\theta dr + \frac{\partial}{\partial t}\int B_{s,x}\sin\theta dr - \frac{J_\theta}{\eta ne}\left[\left(B_{c,x}+B_{s,x}\right)\cos\theta - \left(B_{c,y}+B_{s,y}\right)\sin\theta + B_{ext,r}\right] = \eta J_{z,B_x}. \tag{71}$$

Similarly, KVL for the current that couples to the y-coil, I_{z,B_y} and the current density, J_{z,B_y},

$$\frac{d\left(M_y I_{c,y}\right)}{dt} + \frac{d\left(L_{s,B_x} I_{c,x}\right)}{dt} - \left[\Gamma_{c,(x,y),B_y} I_{c,x} - \Gamma_{c,y} I_{c,y} + \Gamma_{s,(x,y),B_y} I_{s,B_{s,x}} - \Gamma_{s,y} I_{s,B_{s,y}} + \Gamma_{ext,B_x}\right] I_\theta = R_{s,B_x} I_{s,B_y}. \tag{72}$$

$$\frac{\partial}{\partial t}\int B_{c,y}\cos\theta dr + \frac{\partial}{\partial t}\int B_{s,y}\cos\theta dr - \frac{J_\theta}{ne}\left[\left(B_{c,x}+B_{s,x}\right)\cos\theta - \left(B_{c,y}+B_{s,y}\right)\sin\theta + B_{ext,r}\right] = \eta J_{z,B_y}. \tag{73}$$

Indeed, if we add equations 71 and 73, we see that we can rewrite the total current density, J_z, as

$$J_z = J_{z,B_x} + J_{z,B_y} + \frac{J_\theta}{ne}\left[\left(B_{c,x}+B_{s,x}\right)\cos\theta - \left(B_{c,y}+B_{s,y}\right)\sin\theta + B_{ext,r}\right]. \tag{74}$$

3. Deriving Azimuthal Plasma Current Loop Equations

KVL for the azimuthal plasma current can be found in much the same way as the axial plasma currents. We start with the generalized Ohm's law for the azimuthal current density,

$$E_\theta + \frac{J_z B_r}{ne} = \eta J_\theta \tag{75}$$

E_θ is only composed of the time varying electric field caused by the time varying axial magnetic field produced by the azimuthal current,

$$E_\theta = -\frac{\partial}{\partial t}\frac{1}{r}\int rB_{s,z}dr = -\frac{\partial}{\partial t}\frac{1}{r}\int r\gamma_{s,z} I_\theta dr. \tag{76}$$

We plug in equations 63, 70, 74, and 76 into equation 75,

$$-\frac{\partial}{\partial t}\frac{1}{r}\int r\gamma_{s,z} I_\theta dr + \frac{1}{ne}\left(g_{z,B_x} I_{z,B_x} + g_{z,B_y} I_{z,B_y} + \frac{g_\theta I_\theta}{\eta ne}\left[\left(\gamma_{c,x} I_{c,x} + \gamma_{s,x} I_{s,B_x}\right)\cos\theta - \left(\gamma_{c,y} I_{c,y} + \gamma_{s,y} I_{s,B_y}\right)\sin\theta + B_{ext,r}\right]\right)$$
$$\left(\left(\gamma_{c,x} I_{c,x} + \gamma_{s,x} I_{s,B_x}\right)\cos\theta - \left(\gamma_{c,y} I_{c,y} + \gamma_{s,y} I_{s,B_y}\right)\sin\theta + B_{ext,r}\right) = \eta g_\theta I_\theta \tag{77}$$

We multiply by g_θ and integrate over the slug volume, V'. The resulting KVL equation for the azimuthal plasma current is

$$\left(\Gamma'_{c_x,s}I_{c,x} + \Gamma'_{s,B_x}I_{z,B_x} + \Gamma_{ext,B_x}\right)\left(I_{z,B_x} + I_{z,B_y}\right) - \left(\Gamma'_{c_y,s}I_{c,y} + \Gamma'_{s,B_y}I_{z,B_y} - \Gamma_{ext,B_y}\right)\left(I_{z,B_x} + I_{z,B_y}\right) = \frac{d\left(L_{s,\theta}I_\theta\right)}{dt}$$
$$+ (R_{B_ext} + 2R'_{B_{ext},B_{c,x}}I_{c,x} + 2R'_{B_{ext},B_{s,x}}I_{z,B_x} - 2R'_{B_{ext},B_{c,y}}I_{c,y} - 2R'_{B_{ext},B_{s,y}}I_{z,B_y} + R''_{B_{c,x}}I^2_{c,x} + R''_{B_{c,y}}I^2_{c,y}$$
$$+ R''_{B_{s,x}}I^2_{z,B_x} + R''_{B_{s,y}}I^2_{z,B_y} + 2R''_{B_{c,x},B_{s,x}}I_{c,x}I_{z,B_x} - 2R''_{B_{c,x},B_{s,y}}I_{c,x}I_{c,y} - 2R''_{B_{c,x},B_{s,y}}I_{c,x}I_{z,B_y} - 2R''_{B_{c,y},B_{s,x}}I_{c,y}I_{z,B_x}$$
$$+ 2R''_{B_{c,y},B_{s,y}}I_{c,y}I_{z,B_y} - 2R''_{B_{s,x},B_{s,y}}I_{z,B_x}I_{z,B_y} + R_{s,\theta})I_\theta \tag{78}$$

In addition to recovering many of the same gyrator parameters we see in the axial plasma current KVL equations, we get new electrical parameters. Notably, we have additional resistance values that scale with the square of the Hall parameters associated with each radial magnetic field. For the non-classical resistance values in the azimuthal KVL equation, we first define a number of Hall parameters,

$$\Omega_{B_{ext}}{}^2 = \frac{B_{ext,r}{}^2}{(\eta ne)^2} \tag{79}$$
$$\Omega'_{B_{ext},B_{c,x}}{}^2 = \frac{\gamma_{c,x}B_{ext,r}\cos\theta}{(\eta ne)^2} \tag{80}$$
$$\Omega'_{B_{ext},B_{c,y}}{}^2 = \frac{\gamma_{c,y}B_{ext,r}\sin\theta}{(\eta ne)^2} \tag{81}$$
$$\Omega'_{B_{ext},B_{s,x}}{}^2 = \frac{\gamma_{s,B_x}B_{ext,r}\cos\theta}{(\eta ne)^2} \tag{82}$$
$$\Omega'_{B_ext,B_{s,y}}{}^2 = \frac{\gamma_{s,B_y}B_{ext,r}\sin\theta}{(\eta ne)^2} \tag{83}$$
$$\Omega''_{B_{c,x}}{}^2 = \frac{\gamma_{c,B_x}{}^2\cos\theta^2}{(\eta ne)^2} \tag{84}$$
$$\Omega''_{B_{c,y}}{}^2 = \frac{\gamma_{c,B_y}{}^2\sin\theta^2}{(\eta ne)^2} \tag{85}$$
$$\Omega''_{B_{s,x}}{}^2 = \frac{\gamma_{s,B_x}{}^2\cos\theta^2}{(\eta ne)^2} \tag{86}$$
$$\Omega''_{B_{s,y}}{}^2 = \frac{\gamma_{s,B_y}{}^2\sin\theta^2}{(\eta ne)^2} \tag{87}$$
$$\Omega''_{B_{c,x},B_{s,x}}{}^2 = \frac{\gamma_{c,B_x}\gamma_{s,B_x}\cos\theta^2}{(\eta ne)^2} \tag{88}$$
$$\Omega''_{B_{c,x},B_{c,y}}{}^2 = \frac{\gamma_{c,B_x}\gamma_{c,B_y}\cos\theta\sin\theta}{(\eta ne)^2} \tag{89}$$
$$\Omega''_{B_{c,x},B_{s,y}}{}^2 = \frac{\gamma_{c,B_x}\gamma_{s,B_y}\cos\theta\sin\theta}{(\eta ne)^2} \tag{90}$$
$$\Omega''_{B_{c,y},B_{s,x}}{}^2 = \frac{\gamma_{c,B_y}\gamma_{s,B_x}\cos\theta\sin\theta}{(\eta ne)^2} \tag{91}$$
$$\Omega''_{B_{c,y},B_{s,y}}{}^2 = \frac{\gamma_{c,B_y}\gamma_{s,B_y}\sin\theta^2}{(\eta ne)^2} \tag{92}$$
$$\Omega''_{B_{s,x},B_{s,y}}{}^2 = \frac{\gamma_{s,B_x}\gamma_{s,B_y}\cos\theta\sin\theta}{(\eta ne)^2}. \tag{93}$$

These hall parameters are used to define a series of effective resistances that describe the diffusion of the electrons across the total radial magnetic field,

$$R_{B_ext} = \int_{V'} {\Omega_{B_{ext}}}^2 \eta {g_\theta}^2 dV' \tag{94}$$

$$R'_{B_{ext},B_{c,x}} = \int_{V'} {\Omega'_{B_{ext},B_{c,x}}}^2 \eta {g_\theta}^2 dV' \tag{95}$$

$$R'_{B_{ext},B_{c,y}} = \int_{V'} {\Omega'_{B_{ext},B_{c,y}}}^2 \eta {g_\theta}^2 dV' \tag{96}$$

$$R'_{B_{ext},B_{s,x}} = \int_{V'} {\Omega'_{B_{ext},B_{s,x}}}^2 \eta {g_\theta}^2 dV' \tag{97}$$

$$R'_{B_{ext},B_{s,y}} = \int_{V'} {\Omega'_{B_{ext},B_{s,y}}}^2 \eta {g_\theta}^2 dV' \tag{98}$$

$$R''_{B_{c,x}} = \int_{V'} {\Omega''_{B_{c,x}}}^2 \eta {g_\theta}^2 dV' \tag{99}$$

$$R''_{B_{c,y}} = \int_{V'} {\Omega''_{B_{c,y}}}^2 \eta {g_\theta}^2 dV' \tag{100}$$

$$R''_{B_{s,x}} = \int_{V'} {\Omega''_{B_{s,x}}}^2 \eta {g_\theta}^2 dV' \tag{101}$$

$$R''_{B_{s,y}} = \int_{V'} {\Omega''_{B_{c,y}}}^2 \eta {g_\theta}^2 dV' \tag{102}$$

$$R''_{B_{c,x},B_{s,x}} = \int_{V'} {\Omega''_{B_{c,x},B_{s,x}}}^2 \eta {g_\theta}^2 dV' \tag{103}$$

$$R''_{B_{c,x},B_{c,y}} = \int_{V'} {\Omega''_{B_{c,x},B_{c,y}}}^2 \eta {g_\theta}^2 dV' \tag{104}$$

$$R''_{B_{c,x},B_{s,y}} = \int_{V'} {\Omega''_{B_{c,x},B_{s,y}}}^2 \eta {g_\theta}^2 dV' \tag{105}$$

$$R''_{B_{c,y},B_{s,x}} = \int_{V'} {\Omega''_{B_{c,y},B_{s,x}}}^2 \eta {g_\theta}^2 dV' \tag{106}$$

$$R''_{B_{c,y},B_{s,y}} = \int_{V'} {\Omega''_{B_{c,y},B_{s,y}}}^2 \eta {g_\theta}^2 dV' \tag{107}$$

$$R''_{B_{s,x},B_{s,y}} = \int_{V'} {\Omega''_{B_{s,x},B_{s,y}}}^2 \eta {g_\theta}^2 dV' \tag{108}$$

$$\tag{109}$$

4. Slug Acceleration

The acceleration of the slug is defined by Newton's second law. The force acting on the slug is the Lorentz force caused by the azimuthal current interacting with the external radial magnetic field. We can express this Lorentz force as an acceleration constant, β multiplied by the current,

$$m_s \frac{d^2 z}{dt^2} = \beta I_\theta. \tag{110}$$

Here, z is the axial position of the slug and m_s is its mass.

5. Governing system of Equations

Including KVL for the antennae being driven by sinusoidal forcing functions, the full system of equations is

$$V_{C_{t,x}} + L_{c,x}\frac{dI_{c,x}}{dt} + R_{c,x}I_{c,x} - \frac{dM_{c,x}}{dt}I_{z,B_x} - M_{c,x}\frac{dI_{z,B_x}}{dt} = V_0\cos(\omega t) \tag{111}$$

$$V_{C_{t,y}} + L_{c,y}\frac{dI_{c,y}}{dt} + R_{c,y}I_{c,y} - \frac{dM_{c,y}}{dt}I_{z,B_y} - M_{c,y}\frac{dI_{z,B_y}}{dt} = V_0\sin(\omega t) \tag{112}$$

$$\frac{dV_{C_{t,x}}}{dt} = \frac{I_{c,x}}{C_{t,x}} \tag{113}$$

$$\frac{dV_{C_{t,y}}}{dt} = \frac{I_{c,y}}{C_{t,y}} \tag{114}$$

$$\frac{d\left(M_x I_{c,x}\right)}{dt} + \frac{d\left(L_{s,B_x}I_{c,x}\right)}{dt} - \left[\Gamma_{c,x}I_{c,x} - \Gamma_{c,(x,y)}I_{c,y} + \Gamma_{s,x}I_{s,B_{s,x}} - \Gamma_{s,(x,y)}I_{s,B_{s,y}} + \Gamma_{ext,B_x}\right]I_\theta = R_{s,B_x}I_{s,B_x} \tag{115}$$

$$\frac{d\left(M_y I_{c,y}\right)}{dt} + \frac{d\left(L_{s,B_x}I_{c,x}\right)}{dt} - \left[\Gamma_{c,(x,y),B_y}I_{c,x} - \Gamma_{c,y}I_{c,y} + \Gamma_{s,(x,y),B_y}I_{s,B_{s,x}} - \Gamma_{s,y}I_{s,B_{s,y}} + \Gamma_{ext,B_x}\right]I_\theta = R_{s,B_x}I_{s,B_y} \tag{116}$$

$$\begin{aligned}
&\left(\Gamma_{c,x}I_{c,x} - \Gamma_{c,(x,y)}I_{c,y} + \Gamma_{s,x}I_{s,B_{s,x}} - \Gamma_{s,(x,y)}I_{s,B_{s,y}} + \Gamma_{ext,B_x}\right)I_{z,B_x}\\
&\quad + \left(\Gamma_{c,(x,y),B_y}I_{c,x} - \Gamma_{c,y}I_{c,y} + \Gamma_{s,(x,y),B_y}I_{s,B_{s,x}} - \Gamma_{s,y}I_{s,B_{s,y}} + \Gamma_{ext,B_x}\right)I_{z,B_y} = \frac{d\left(L_{s,\theta}I_\theta\right)}{dt}\\
&\quad + (R_{B_ext} + 2R'_{B_{ext},B_{c,x}}I_{c,x} + 2R'_{B_{ext},B_{s,x}}I_{z,B_x} - 2R'_{B_{ext},B_{c,y}}I_{c,y} - 2R'_{B_{ext},B_{s,y}}I_{z,B_y} + R''_{B_{c,x}}I_{c,x}^2 + R''_{B_{c,y}}I_{c,y}^2\\
&\quad + R''_{B_{s,x}}I_{z,B_x}^2 + R''_{B_{s,y}}I_{z,B_y}^2 + 2R''_{B_{c,x},B_{s,x}}I_{c,x}I_{z,B_x} - 2R''_{B_{c,x},B_{s,y}}I_{c,x}I_{c,y} - 2R''_{B_{c,x},B_{s,y}}I_{c,x}I_{z,B_y} - 2R''_{B_{c,y},B_{s,x}}I_{c,y}I_{z,B_x}\\
&\quad + 2R''_{B_{c,y},B_{s,y}}I_{c,y}I_{z,B_y} - 2R''_{B_{s,x},B_{s,y}}I_{z,B_x}I_{z,B_y} + R_{s,\theta})I_\theta
\end{aligned} \tag{117}$$

$$m_s\frac{d^2z}{dt^2} = \beta I_\theta. \tag{118}$$

This is the full system of equations before assumptions are applied.

References

[1] Blevin, H. A., and Thonemann, P. C., "Plasma confinement using an alternating magnetic field," *Conference on Plasma Physics and Controlled Nuclear Fusion Research, Nuclear Fusion Supplement, Part 1*, 1962, pp. 55–60.

[2] Hugrass, W. N., Jones, I. R., McKenna, K. F., Phillips, M. G. R., Storer, H. G., and Tuczek, H., "Compact Torus Configuration Generated by a Rotating Magnetic Field: The Rotamak," *Physical Review Letters*, Vol. 44, No. 25, 1980, pp. 1676–1679. https://doi.org/10.1103/PhysRevLett.44.1676.

[3] Hugrass, W. N., Okada, T., and Ohnishi, M., "Plasma-circuit Interactions in Rotating Magnetic Field Current Drive," *Plasma Physics and Controlled Fusion*, Vol. 50, 2008, p. 055008. https://doi.org/10.1088/0741-3335/50/5/055008.

[4] Jankovsky, R., Tverdokhlebov, S., and Manzella, D., "High Power Hall Thrusters," *35th Joint Propulsion Conference*, 1999, pp. AIAA–99–315745.

[5] Jahn, R. G., *Physics of Electric Propulsion*, McGraw-Hill, New York, 1968.

[6] Polzin, K., Martin, A., Little, J., Promislow, C., Jorns, B., and Woods, J., "State-of-the-Art and Advancement Paths for Inductive Pulsed Plasma Thrusters," *Aerospace*, Vol. 7, No. 8, 2020, p. 105. https://doi.org/10.1103/PhysRevLett.107.235001.

[7] Hill, C. S., "Translation studies on an annular field reversed configuration device for space propulsion," Ph.D. thesis, Michigan Technological University, 2012.

[8] Slough, J., Kirtley, D., and Weber, T., "Pulsed plasmoid propulsion: The ELF thruster," *31st International Electric Propulsion Conference*, 2009. IEPC paper 2009-265.

[9] Weber, T., "The electrodeless Lorentz force thruster experiment," Ph.D. thesis, University of Washington, 2010.

[10] Woods, J. M., Sercel, C. L., Gill, T. M., and Jorns, B. A., "Performance Measurements of a Rotating Magnetic Field Thruster," *AIAA Propulsion and Energy Forum*, VIRTUAL, 2020.

[11] Sercel, C. L., Woods, J. M., Gill, T. M., and Jorns, B. A., "Impact of Flux Conservers on Performance of Inductively Driven Pulsed Plasmoid Thrusters," *AIAA Propulsion and Energy Forum*, VIRTUAL, 2020.

[12] Sercel, C. L., Woods, J. M., Gill, T. M., and Jorns, B. A., "Performance Measurements of a 5 kW-Class Rotating Magnetic Field Thruster," *AIAA Propulsion and Energy Forum*, VIRTUAL, 2021.

[13] Weber, T. E., Slough, J. T., and Kirtley, D., "The electrodeless Lorentz force (ELF) thruster experimental facility," *Review of Scientific Instruments*, Vol. 83, No. 11, 2012, p. 113509. https://doi.org/10.1063/1.4759000.

[14] Little, J., Cornella, B., Pancotti, A., and Kirtley, D., "Scaling of FRC Thrusters with Neutral Entrainment," *8th Joint Army-Navy-NASA-Air Force (JANNAF) Spacecraft Propulsion Subcommittee Meeting*, 2016.

[15] Woods, J. M., Jorns, B. A., and Gallimore, A. D., "Circuit Modeling of Rotating Magnetic Field Field-reversed Configuration Thrusters," *AIAA Propulsion and Energy Forum*, 2018. https://doi.org/10.2514/6.2018-4911, aIAA paper 2018-4911.

[16] Woods, J. M., Sercel, C. L., Gill, T. M., Viges, E., and Jorns, B. A., "Data-Driven Approach to Modeling and Development of a 30 kW Field-reversed Configuration Thruster," *36th International Electric Propulsion Conference*, 2019. IEPC paper 2019-717.

[17] Polzin, K. A., "Scaling and systems considerations in pulsed inductive plasma thrusters," *IEEE Transactions on Plasma Science*, Vol. 36, No. 5, 2008, pp. 2189–2198. https://doi.org/10.1109/TPS.2008.2003537.

[18] Martin, A. K., and Eskridge, R. H., "Electrical coupling efficiency of inductive plasma accelerators," *Journal of Physics D: Applied Physics*, Vol. 38, No. 23, 2005, pp. 4168–4179. https://doi.org/10.1088/0022-3727/38/23/005.

[19] Niemela, C. S., and King, L. B., "Numerical Optimization of an Annular Field Reversed Configuration Translation Experiment," *31st International Electric Propulsion Conference*, 2009. IEPC paper 2009-008.

[20] Adams, K., Deprettere, E., and Voorman, J., "The Gyrator in Electronic Systems," Academic Press, 1975, pp. 79–179. https://doi.org/https://doi.org/10.1016/S0065-2539(08)60537-5, URL https://www.sciencedirect.com/science/article/pii/S0065253908605375.

[21] Polzin, K. A., and Choueiri, E. Y., "Performance optimization criteria for pulsed inductive plasma acceleration," *IEEE Transactions on Plasma Science*, Vol. 34, No. 3, 2006, pp. 945–953. https://doi.org/10.1109/TPS.2006.875732.

[22] Eskridge, R. H., Fimognari, P. J., Martin, A. K., and Lee, M. H., "Design and Construction of the PT-1 Prototype Plasmoid Thruster," *AIP Conference Proceedings*, Vol. 813, 2006, p. 474. https://doi.org/10.1063/1.2169225.

[23] Wong, A. R., Toftul, A., Polzin, K. A., and Pearson, J. B., "Non-contact thrust stand calibration method for repetitively pulsed electric thrusters," *Review of Scientific Instruments*, Vol. 83, No. 2, 2012, p. 025103. https://doi.org/10.1063/1.3680557.

[24] Viges, E. A., Jorns, B. A., Gallimore, A. D., and Sheehan, J. P., "University of Michigan's Upgraded Large Vacuum Test Facility," *36th International Electric Propulsion Conference*, 2019. IEPC-2019-653.

[25] Takahashi, K., "Helicon-type radiofrequency plasma thrusters and magnetic plasma nozzles," *Reviews of Modern Plasma Physics*, Vol. 3, No. 3, 2019. https://doi.org/10.1007/s41614-019-0024-2.